Cortical neuronal assemblies coordinate with EEG microstate dynamics during resting wakefulness

Richard Boyce, Robin F Dard, Rosa Cossart

Report

Cell Reports

Cortical neuronal assemblies coordinate with EEG microstate dynamics during resting wakefulness

Graphical abstract

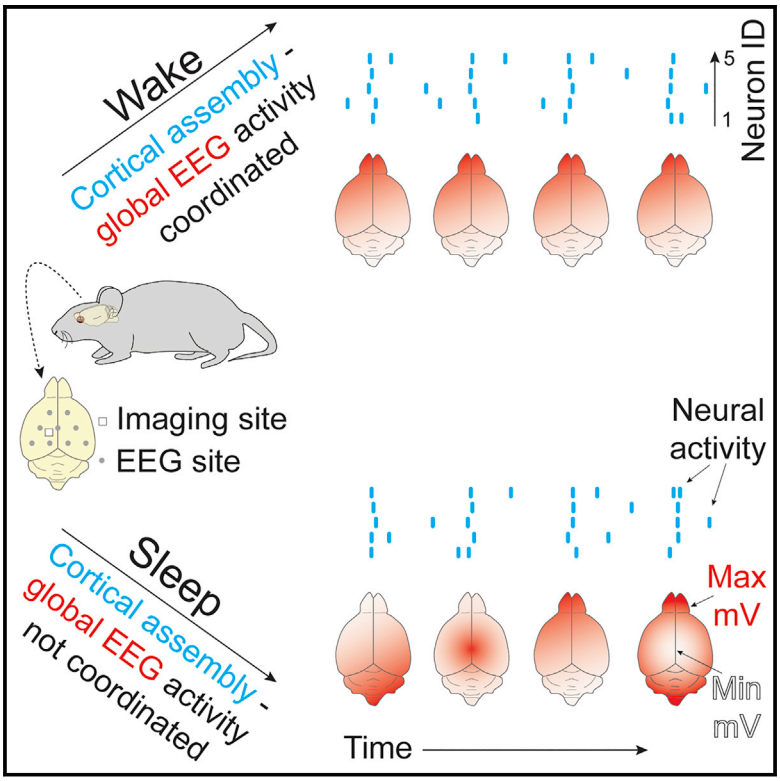

Highlights

- The somatosensory cortex is imaged across the full sleep-wake cycle in mice
- Cortical neural assembly activity is not different during quiet wake vs. sleep
- Assembly activity is only coordinated with global brain dynamics during wake

Authors

Richard Boyce, Robin F. Dard, Rosa Cossart

Correspondence

rboyce54@gmail.com

In brief

Boyce et al. show that local cortical neural assembly activity coordinates with global brain dynamics during wakefulness, but not during sleep, when consciousness is significantly reduced. This suggests that the coordination of local cortical assembly activity with global brain dynamics may be a key mechanism behind sustained conscious experience.

Boyce et al., 2023, Cell Reports *42*, 112053
February 28, 2023
https://doi.org/10.1016/j.celrep.2023.112053

CellPress

Cell Reports

CellPress
OPEN ACCESS

Report

Cortical neuronal assemblies coordinate with EEG microstate dynamics during resting wakefulness

Richard Boyce,[1,2,*] Robin F. Dard,[1] and Rosa Cossart[1]
[1]INMED, INSERM, Aix Marseille University, 13273 Marseille, France
[2]Lead contact
*Correspondence: rboyce54@gmail.com
https://doi.org/10.1016/j.celrep.2023.112053

SUMMARY

The disruption of cortical assembly activity has been associated with anesthesia-induced loss of consciousness. However, the relationship between cortical assembly activity and the variations in consciousness associated with natural vigilance states remains unclear. Here, we address this by performing vigilance state-specific clustering analysis on 2-photon calcium imaging data from the sensorimotor cortex in combination with global electroencephalogram (EEG) microstate analysis derived from multi-EEG signals obtained over widespread cortical locations. We report no difference in the structure of assembly activity during quiet wakefulness (QW), non-rapid eye movement sleep (NREMs), or REMs, despite the latter two vigilance states being associated with significantly reduced levels of consciousness relative to QW. However, we describe a significant coordination between global EEG microstate dynamics and general local cortical assembly activity during periods of QW, but not sleep. These results suggest that the coordination of cortical assembly activity with global brain dynamics could be a key factor of sustained conscious experience.

INTRODUCTION

Neural assemblies, groups of neurons that coactivate together, have long been suggested to play an important role in cognition.[1–5] Several decades ago, the presence and proposed importance of assemblies in brain function began to find more experimental support due to advances in electrode recording techniques that enabled data to be obtained from large numbers of neurons spread over relatively localized brain regions.[6] Such experiments were able to detect statistical features indicative of the presence of assembly organization.[7–9] More recently, the development of genetically encoded calcium indicators and optogenetic techniques in combination with 2-photon imaging platforms has allowed for the observation and manipulation of cortical neurons with a more optimal spatial resolution. Resulting experiments have enabled the direct visualization of localized microcircuit-level cortical assembly activity in mice *in vivo*,[10] confirmed long-theorized properties attributed to microcircuit-level cortical assemblies such as pattern completion,[11] and demonstrated their importance in various cortical regions to associated learning behaviors.[12,13]

The above results have cumulatively helped to establish local microcircuit-level cortical assemblies as critical units involved in cognitive tasks such as learning. However, the more general question of their relationship with consciousness remains unclear. Using 2-photon imaging of layer 2/3 sensorimotor cortex in a head-fixed mouse model, a recent study was able to gain insight into local microcircuit-level cortical assembly dynamics in the awake vs. anesthetized unconscious state.[14] The authors reported that the onset of general anesthesia was associated with a reversible reduction and fragmenting of assemblies, suggesting their potential role in maintaining consciousness and, more generally, supporting the hypothesis that cortical assemblies are unitary components of cognition.[2,3] However, there is currently a lack of information about local microcircuit-level cortical assembly dynamics across the full range of natural vigilance states, including sleep (non-rapid eye movement sleep [NREMs] and REMs), when consciousness is significantly reduced relative to waking behaviors.[15] If intact local microcircuit-level cortical assembly activity is a key component of consciousness, then this structured activity might also be expected to be altered to some extent during sleep.

To help improve our understanding of the potential role of local microcircuit-level cortical assemblies in consciousness, we have performed 2-photon calcium imaging of the sensorimotor cortex in combination with multi-electroencephalogram (EEG) recordings across the full sleep-wake cycle in fully habituated head-fixed mice. Our initial aim was to compare and contrast the characteristics of local microcircuit-level assemblies occurring during each vigilance state in order to gain greater insight into their potential role in conscious experience.

RESULTS

Imaging sensorimotor cortex across the full sleep-wake cycle

To facilitate stable long-term imaging of cortical neural activity, we injected an adeno-associated viral vector encoding the calcium indicator GCaMP6s driven under the hSyn promoter into the left ventricle of neonatal mice. The resulting brain-wide expression of GCaMP6s was stable well into adulthood

(at least 6 months post-injection) (Figures 1A and 1B, top right), as previously reported.[16,17]

We next habituated previously injected adult mice to sleep on a head-fixed, non-motorized treadmill setup (Figures 1A, 1B, S1A, S1B, S2, method details). Layer 2/3 of the sensorimotor cortex was subsequently imaged through a window placed on the overlying dura in head-fixed mice during recording sessions in order to determine the characteristics of cortical assemblies across different vigilance states. Because 2-photon microscopy imaging produced noise and necessarily took place in a dark and open-concept space, the sleep-wake structure was altered (sleep activity reduced) relative to established baseline norms (i.e., in a quiet home cage during the light cycle[18]); however, we were still able to detect clear wake and sleep states.

Detection of vigilance state-specific local microcircuit-level assembly activity in sensorimotor cortex

Calcium trace-derived activity raster plots for a total of 1,290 neurons from 6 mice (average = 215 ± 34 neurons/mouse) were extracted from the imaged movies (Figure 2A). For use in all subsequent analysis, we isolated equal amounts of data for each of 4 vigilance states: active wakefulness (AW), quiet wakefulness (QW), NREMs (N), and REMs (R). Our first analysis focused on the activity of individual neurons. The proportion of cells active during periods of AW was significantly higher than for all other states, with the majority of all cells being active for at least 1 frame during the analysis period (AW = 84% ± 3%; QW = 36.4% ± 10.3%; N = 41.5% ± 11.7%; R = 43.8% ± 11.5%). Similarly, basic activity rates, measured as the number of active frames/second, were generally higher during periods of AW relative to all other states, with a significant difference in mean activity rate at the group level being found between AW and QW (AW = 0.65 ± 0.18; QW = 0.10 ± 0.01; N = 0.15 ± 0.03; R = 0.20 ± 0.05, AW vs. QW $p < 0.01$; Kruskall-Wallis test with Dunn's multiple comparisons test; Figures 2Ci-ii). Neither of the above measures were significantly different between periods of QW, N, and R, in line with prior work.[19]

We next analyzed the activity of vigilance state-specific local microcircuit-level cortical assemblies, defined here as groups of local cortical neurons that coactivate together, using a hierarchical clustering method (method details). We were able to identify significant assembly activity in data from every vigilance state of each experiment (Figure 2B). There was no difference between vigilance states in the number of assemblies identified (Figures 2Ciii); however, there were significantly more neurons/assembly during AW relative to QW, N, and R periods, which were indifferent from one another (Figures 2Civ). We then measured assembly activity during the different vigilance states (method details), with no significant difference found in the number of assembly activations between any of the vigilance states tested (Figures 2Cv). Assessment of the relationship between constituent neurons of assemblies (i.e., assembly similarity) identified during different vigilance states within experiments revealed no consistent indication of similarity above chance levels for any vigilance state pair (Figures S3B and S3C).

Identification of global EEG microstates from multi-EEG recordings during different vigilance states

While our result of having found no clear consistent differences in the structural characteristics of local microcircuit-level cortical assembly activity between QW, N, and R behaviors could be inconsistent with the idea that they are critically involved in consciousness, we hypothesized that there might be a difference in the coordination of assembly activity with global brain dynamics. Indeed, recent evidence has indicated that while local patterns of general network activity are preserved,[20,21] disrupted functional connectivity and coordination between distant cortical regions is a hallmark of the anesthetized brain.[21–23] An established approach that has provided much insight into macroscale brain dynamics involves analyzing how the relationship between EEG recordings obtained simultaneously from widespread cortical locations changes over time.[24–27] Specifically, this procedure involves clustering topographical EEG potential profiles during moments of peak variability between the EEG signals and has consistently demonstrated that global EEG activity dynamically shifts between a relatively small number of quasi-stable configurations. Termed "EEG microstates," such dynamics on the global EEG scale have attracted significant interest in recent years due to their potential involvement in general cognition and conscious experience.[28–31] We therefore next sought to investigate the coordination of local microcircuit-level cortical assembly activity with global brain dynamics in a subset of 3 mice that had been implanted with multi-EEGs (Figure 3A). We first clustered topographical EEG potential profiles from data corresponding to periods of peak variation between EEGs during the same time periods used for imaging-derived assembly analysis in the sensorimotor cortex for QW, N, and R. AW periods were not analyzed due to the strong possibility of contamination of EEG signals by movement-related artifacts. Significant clustering of EEG topographies was found for all vigilance states tested in each experiment, with an optimal cluster number of 4 being consistently indicated for all vigilance states in each experiment (Figures S4A and S4B). The ordered sets of EEG potential profile maps (microstate maps 1–4) derived from the optimal cluster definitions were similar between different vigilance states within an experiment (mean Pearson r values: QW-N = 0.79 ± 0.08; QW-R = 0.91 ± 0.01; N-R = 0.83 ± 0.07; Figures S5A and S5B; Table S1). Microstate maps were also positively correlated between experiments (mean inter-experiment Pearson r values: QW = 0.80 ± 0.07; N = 0.68 ± 0.10; R = 0.41 ± 0.10; Figures S5A and S5B; Table S2). To gain insight into the dynamics of EEG microstates, we next correlated each microstate map with instantaneous EEG potentials at each time point of the data segments (Figure 3B). Microstates were found to cycle dynamically during all states; however, spectral analysis revealed that the main frequencies at which this cycling occurred differed depending on vigilance state (Figure 3C). Spectra for both QW and N were dominated by peaks in the delta (1–4 Hz) frequency range (mean dominant frequency: QW = 3 ± 0.4 Hz; N = 3.6 ± 0.3 Hz), although transient spindle oscillation-associated (9–15 Hz) higher-frequency dynamics during select N data were sometimes observed (Figure S6). In contrast, spectra for

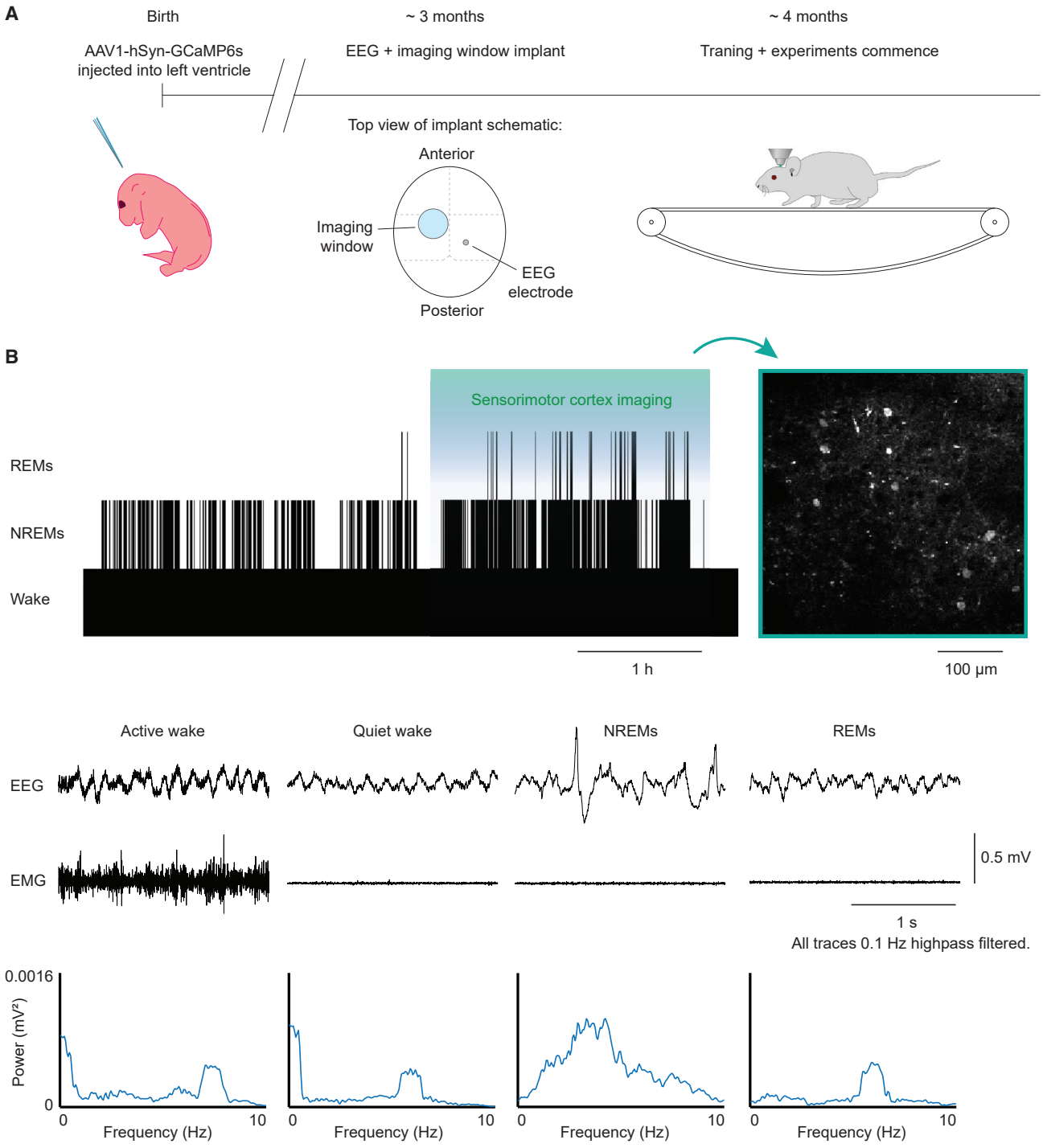

Figure 1. Imaging sensorimotor cortex across the full sleep-wake cycle

(A) Experimental timeline. Left: an adeno-associated viral vector encoding the calcium indicator GCaMP6s driven under the hSyn promoter was injected into the left ventricle of neonatal mice (P0). Center: ~3 months later, mice were implanted with an imaging window and EEG and EMG electrodes used to assess sleep activity. Right: following recovery from surgery, mice were trained to sleep on a non-motorized treadmill in order to image sensorimotor cortex across the full sleep-wake cycle. (B) Top: example hypnogram showing the general imaging procedure in habituated mice. GCaMP6s expression resulting from P0 injection was widespread and stable long term throughout the cortex, allowing for high-quality imaging data acquisition from sensorimotor cortex months after the initial injection. Imaging data acquisition was completed during the second half of each experimental session when sleep activity was highest. Middle: example EEG and electromyogram (EMG) traces from major vigilance states analyzed in this study. Bottom: spectral analysis derived from 5 s time epochs centered around the example EEG traces above. Analysis of the EEG spectrum, EMG activity, and behavioral observation were used to determine vigilance states throughout the entire course of experiments (method details).

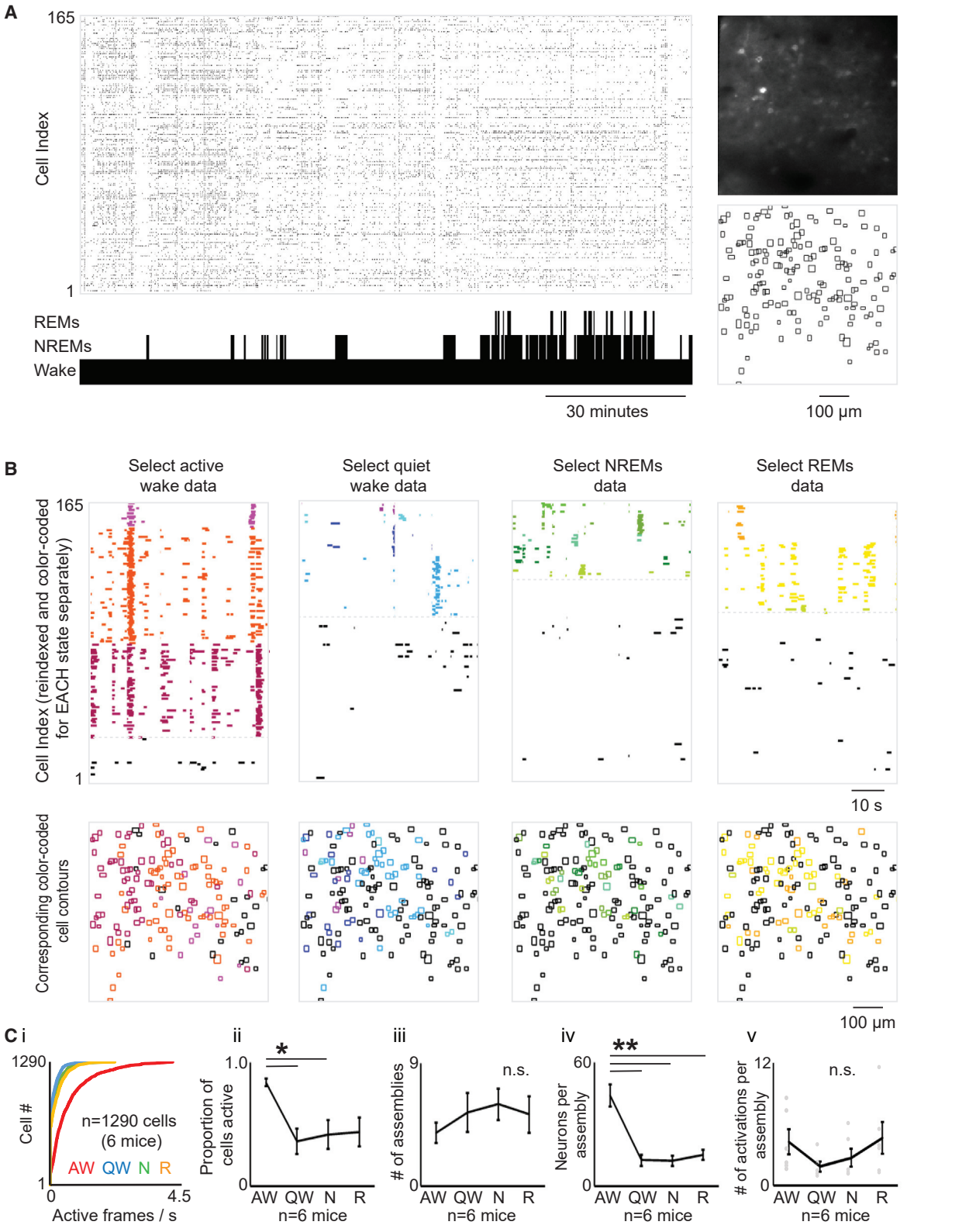

(legend on next page)

R data peaked in the theta (4–10 Hz) range (mean dominant frequency: R = 6.3 ± 0.2 Hz). Correlation analysis between microstate dynamics and each individual EEG channel indicated that no single EEG exerted disproportionate influence over microstate dynamics (Table S3). We also correlated microstate dynamics vs. the average complex wavelet transform across all EEGs at each time point and found that microstate dynamics were not influenced by changes in global oscillation strength for any of the standard frequency bands tested (Table S4). Thus, our results are in general agreement with those described previously.[24–28]

Microcircuit-level assembly activity in sensorimotor cortex is coordinated with global EEG microstates during QW

To investigate the potential relationship between EEG microstate dynamics and local microcircuit-level assembly activity in the sensorimotor cortex, we next calculated the locations of estimated cortical assembly activation start points during QW and N separately for each experiment (Figures 4A and 4B; method details). Values for R were not calculated because the dominant frequency of microstate dynamics during this vigilance state was not less than the Nyquist frequency of imaging data (1/2 the imaging frame rate [8 Hz]), which would have been susceptible to under sampling as a result. The correlation coefficient *r* values calculated for each EEG microstate map corresponding to the 125 ms (∼imaging frame rate) periods before and after the estimated start point were then determined for each assembly activation and average values calculated for each vigilance state tested. We found that *r* values corresponding to EEG microstate maps 1 and 2, associated with relatively increased potentials in frontal and posterior EEGs, in the 125 ms period following estimated assembly activations were significantly higher relative to the preceding 125 ms time window during QW. In contrast, no such differences were found for assembly activations during N periods (Figures 4B, 4C, and S7, top middle). To ensure that this result was not due to under sampling of imaging data during transient spindle-associated periods of increased frequency EEG microstate dynamics during N periods, we next automatically detected spindle activity in all EEGs (Figure S6). Spindle activity coincidence, defined as significant spindle activity being detected in at least 1 EEG channel during the −125:+125 ms peri-assembly activation period, was only found to occur in a minority (11%) of assembly activations; the removal of these data points did not significantly alter our results (Figure S7, bottom).

DISCUSSION

Our results suggest that the general coordination of local microcircuit-level cortical assembly activity with global brain dynamics could be key for sustaining a stable state of consciousness, whereas the mere presence of cortical assemblies is necessary[14] but not sufficient. Our results are also in line with prior experiments which have demonstrated that while local patterns of general network activity can be preserved[20,21] (but see also),[14] disrupted coordination between distant cortical regions is observed during anesthesia-induced unconscious states.[21–23]

In this study, we employed EEG microstate analysis as a method to gain insight into global brain dynamics. While this analysis is derived from cortical EEG signals, the brain-wide relevance of EEG microstate dynamics has been suggested by prior studies that associated them to resting state networks in dual EEG-fMRI experiments,[32–34] as well as studies that used source localization techniques to reveal multiple underlying contributors to the EEG signal.[35,36,37] Furthermore, a similar "EEG microstate" analysis approach was applied to data obtained from high-density electrode arrays implanted in the prefrontal cortex, striatum, and ventral tegmental area in a recent study utilizing a rat model.[38] The authors reported that each brain region produced dynamics that were similar to those of more traditional EEG studies. Cumulatively, these studies suggest that EEG microstate dynamics may directly reflect transient alterations in the functional connectivity between a variety of different brain regions, although currently, little is known of their direct relation to underlying neural activity.[27] Thus, our study also provides important insight by demonstrating the relationship between local microcircuit-level cortical assembly activity and EEG microstate dynamics during periods of restful wake. More generally, our data suggest that EEG microstates could be a mechanism by which local microcircuits are able to coordinate across relatively distant brain regions in the awake brain. Our present work thus highlights a promising direction of research with potentially significant implications considering, aside from their potential role in general cognition and conscious experience,[28–31] the possible association between aberrant microstate dynamics and neuropsychiatric disorders, most notably schizophrenia,[39–47] among others.[43,48–54]

From a more general perspective, our data provides evidence that EEG microstates could play an important mechanistic role in promoting coordination and temporary binding between local activity patterns in relatively distant and physically segregated neural populations at the microcircuit level in the awake resting brain, although this remains to be tested. Future work is also required to more fully explore the possible mechanisms,

Figure 2. Detection of vigilance state-specific local microcircuit-level assembly activity in sensorimotor cortex

(A) Example activity raster from an imaging experiment (black = active). The hypnogram at the bottom indicates the behavioral state at a given time point. Top right: imaging frame taken from the experiment showing the field of view in the sensorimotor cortex. Bottom right: neuron contours obtained from the field of view.

(B) Sample vigilance state-specific hierarchical clustering results obtained from select data originating from the raster shown in (A). For each vigilance state, significant assemblies identified have had their constituent neurons reindexed and color coded for clarity. Cells plotted below the faded gray line were not clustered into a significant assembly. Bottom: vigilance state-specific neuron contour plots with color coding corresponding to the raster plots above.

(Ci–Cv) Group-level analyses of basic cortical neuron and assembly activity from select data obtained for each vigilance state. (i) Plots of inferred firing rate distributions for all neurons pooled across experiments. (ii) Mean proportion of cells that were active for at least 1 frame during select data. (iii) Mean number of significant assemblies identified. (iv) Mean number of constituent cells/assembly. (v) Mean number of assembly activations (gray dots representing individual data values included due to large SEM) (n = 6; n.s., not significant, *p < 0.05, **p < 0.01, one-way repeated measures ANOVA with Tukey's multiple comparisons post-hoc test, ii–iv/Kruskal-Wallis test with Dunn's multiple comparisons post-hoc test, v). Data are represented as mean ± SEM.

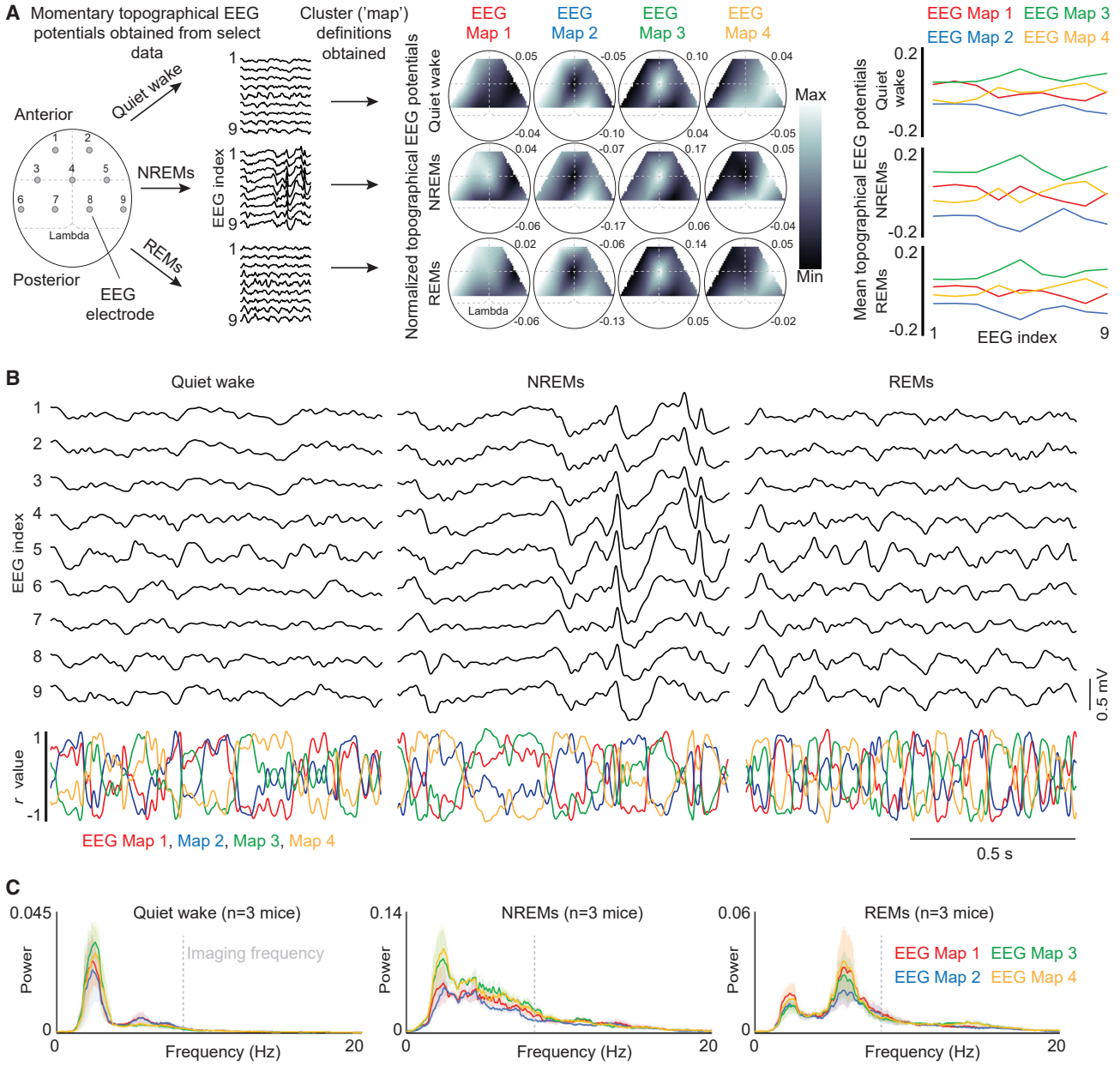

Figure 3. Identification of global EEG microstates from multi-EEG recordings during different vigilance states

(A) Schematic of EEG microstate detection procedure. Left: multi-EEG signals originating from EEG electrodes widely spread over the cortical surface were obtained for the same select quiet wakefulness (QW), N, and R time periods used for imaging data analysis. Imaging window not included in the dorsal-view schematic for clarity. The topographical EEG potential profiles were then clustered at specific time points, resulting in the identification of significant clusters (Figure S4; method details). Center: example normalized topographical EEG profile "microstate maps," scaled with max-min difference for each map individually to enable visualization of variations in topographical potentials within each given map (method details), derived from optimal significant cluster definitions identified in prior clustering steps for one experiment. Numerical values to the immediate top/bottom right indicate the maximum/minimum bounds (mV) of the scale used for each individual plot. Right: a single graph with a common scale containing linear plots of the same corresponding derived EEG potential values that were used to generate topographical maps are shown to provide direct comparison of the potential values associated with different maps.

(B) Top: expanded example of multi-EEG data plots for each vigilance state analyzed. Bottom: corresponding plots of Pearson correlation *r* values calculated between momentary multi-EEG topographical profiles and microstate map templates (identified in A) used to show the relationship between multi-EEG data and EEG microstate dynamics.

(C) Group-level spectral analyses of identified global EEG microstate dynamics (Pearson correlation *r* values calculated between momentary multi-EEG topographical profiles and microstate map templates at each data point). Note the different linear scales on the y axis.

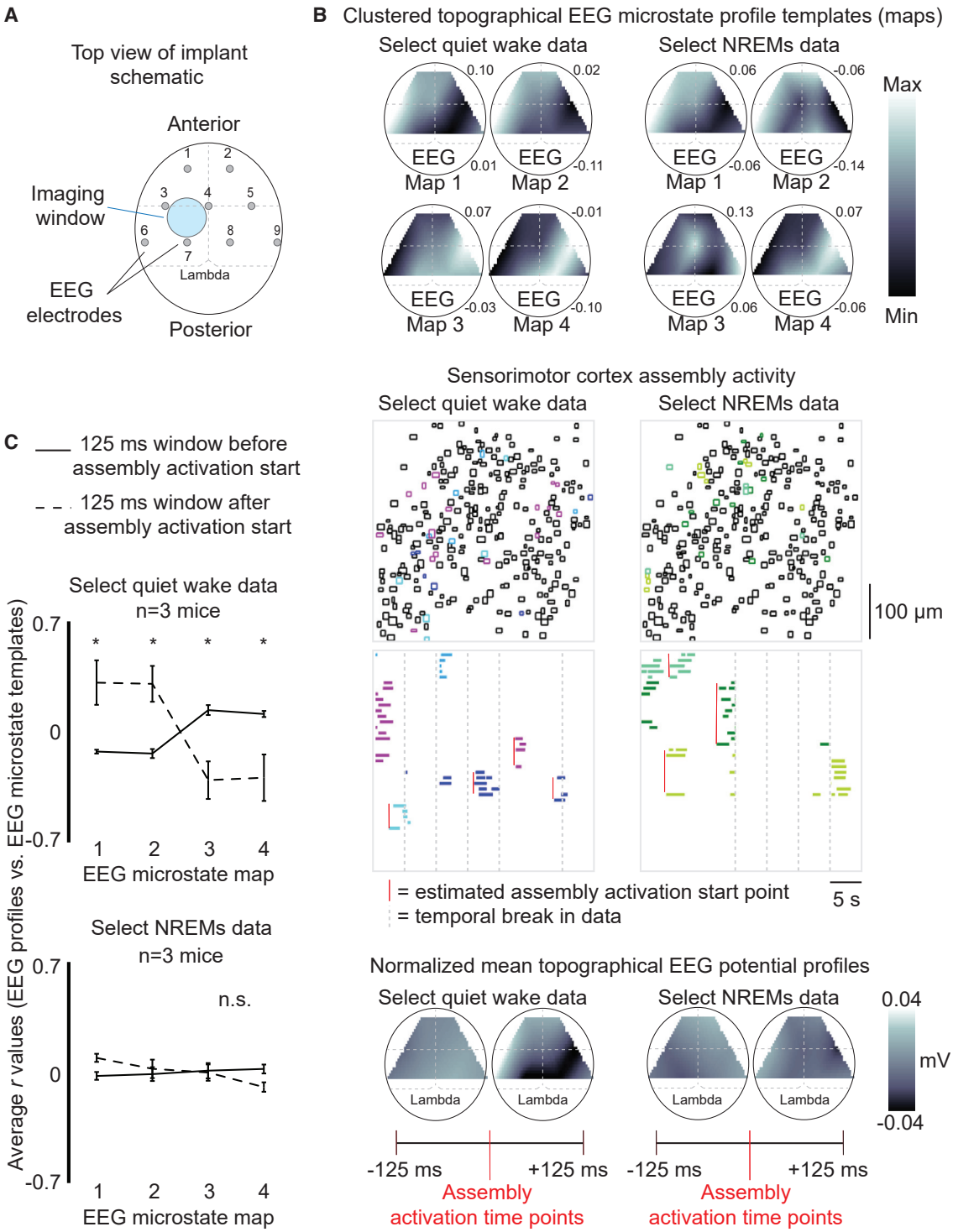

Figure 4. Microcircuit-level assembly activity in sensorimotor cortex is coordinated with global EEG microstates during QW

(A) Dorsal schematic of the implant allowing for simultaneous imaging of the sensorimotor cortex and multi-EEG recording.

(B) Example of vigilance state-specific correspondence between EEG microstate dynamics and microcircuit-level assembly activity in the sensorimotor cortex. Top: sample normalized EEG microstate template maps generated for select quiet wake and NREMs data from experiment ID058 (Figure S5B). Numerical values to the immediate top/bottom right indicate the maximum/minimum bounds (mV) of the scale used for each individual plot. Middle: color-coded contour maps and corresponding spike rasters obtained from the same select data periods as the above EEG microstate maps. To assess the relationship between microcircuit-level assembly activity and global EEG microstate dynamics during QW and NREMs, the estimated start points of assembly activations were obtained (red

(legend continued on next page)

including directionality, behind the coordination between global brain dynamics and microcircuit-level assembly activity that we observed in the awake resting brain.

Limitations of the study

The relatively low temporal resolution of calcium imaging limited our ability to fully resolve the finer structure of identified cortical assembly activity and prevented us from analyzing the potential relationship between cortical microcircuit-level assembly activity and EEG microstate dynamics during R.

The hierarchical clustering procedure used to identify significant cortical assemblies can only assign a given neuron to 1 cluster. Therefore, neurons that may participate in multiple clusters are not considered in this study.

STAR★METHODS

Detailed methods are provided in the online version of this paper and include the following:

- KEY RESOURCES TABLE
- RESOURCE AVAILABILITY
  - Lead contact
  - Materials availability
  - Data and code availability
- EXPERIMENTAL MODEL AND SUBJECT DETAILS
- METHOD DETAILS
  - Virally-mediated expression of calcium indicators
  - Implantation of electrodes and imaging window
  - Habituation to head fixation
  - Electrophysiological recording
  - 2-Photon imaging of cortical neural activity
  - Data analysis
  - Vigilance state architecture analysis
  - Spectral analysis of EEG data
  - Wavelet analysis of EEG data
  - EEG microstate analysis
  - Construction of topographical maps of multi-EEG potentials
  - Analysis of spindle activity in multi-EEG data
  - Motion correction of imaging data
  - Determination of neurons (regions of interest) in imaging field of view
  - Identification of transient activity in calcium traces
  - Hierarchical clustering of cortical imaging data
- QUANTIFICATION AND STATISTICAL ANALYSIS

SUPPLEMENTAL INFORMATION

Supplemental information can be found online at https://doi.org/10.1016/j.celrep.2023.112053.

ACKNOWLEDGMENTS

R.B. was supported by The International Human Frontier Science Program Organisation (HFSP) postdoctoral fellowship #LT000835/2018-L. This project received support from ERC Neuropioneers (grant number 646925 - ERC-2014-CoG), the Fondation Bettencourt Schueller, and ERC Hope (grant NUMBER 95133 - ERC Synergy Grants 2020).

AUTHOR CONTRIBUTIONS

R.B. conceived and designed the research project, completed surgical implantation procedures and subsequent experiments in adult mice, performed all data analysis, and wrote the manuscript. R.F.D. performed intraventricular virus injections in mouse pups. R.C. established the laboratory in which experiments were completed, supervised the study, and provided financial support.

DECLARATION OF INTERESTS

The authors declare no competing interests.

Received: June 13, 2022
Revised: September 26, 2022
Accepted: January 17, 2023
Published: January 29, 2023

REFERENCES

1. Lorente de Nó, R. (1933). Studies on the structure of the cerebral cortex. I. The area entorhinalis. J. Psychol. Neurol. *45*, 381–438.
2. Hebb, D.O. (1949). The Organization of Behavior; a Neuropsychological Theory (Wiley). https://doi.org/10.1016/s0361-9230(99)00182-3.
3. Hopfield, J.J. (1982). Neural networks and physical systems with emergent collective computational abilities. Proc. Natl. Acad. Sci. USA *79*, 2554–2558. https://doi.org/10.1073/pnas.79.8.2554.
4. Harris, K.D. (2005). Neural signatures of cell assembly organization. Nat. Rev. Neurosci. *6*, 399–407. https://doi.org/10.1038/nrn1669.
5. Buzsáki, G. (2010). Neural syntax: cell assemblies, synapsembles, and readers. Neuron *68*, 362–385. https://doi.org/10.1016/j.neuron.2010.09.023.
6. Carrillo-Reid, L., and Yuste, R. (2020). Playing the piano with the cortex: role of neuronal ensembles and pattern completion in perception and behavior. Curr. Opin. Neurobiol. *64*, 89–95. https://doi.org/10.1016/j.conb.2020.03.014.
7. Wilson, M.A., and McNaughton, B.L. (1993). Dynamics of the hippocampal ensemble code for space. Science *261*, 1055–1058. https://doi.org/10.1126/science.8351520.
8. Harris, K.D., Csicsvari, J., Hirase, H., Dragoi, G., and Buzsáki, G. (2003). Organization of cell assemblies in the hippocampus. Nature *424*, 552–556. https://doi.org/10.1038/nature01834.
9. Truccolo, W., Hochberg, L.R., and Donoghue, J.P. (2010). Collective dynamics in human and monkey sensorimotor cortex: predicting single neuron spikes. Nat. Neurosci. *13*, 105–111. https://doi.org/10.1038/nn.2455.
10. Miller, J.e.K., Ayzenshtat, I., Carrillo-Reid, L., and Yuste, R. (2014). Visual stimuli recruit intrinsically generated cortical ensembles. Proc. Natl. Acad. Sci. USA *111*, E4053–E4061. https://doi.org/10.1073/pnas.1406077111.

vertical lines). Bottom: the mean topographical EEG potentials were then calculated for the 125 ms windows immediately prior to and after each valid assembly activation. Averaged topographical potential values are shown in the plots. Monotone plots during the 125 ms windows both preceding and following valid assembly activations in NREMs data are indicative of relatively reduced correspondence between microcircuit-level assembly activation time points and EEG microstate dynamics compared with quiet wake.

(C) Group-level analysis of Pearson correlation *r* values calculated between momentary multi-EEG topographical profiles and microstate map templates at each data point within the ±125 ms windows surrounding assembly activation start points (n.s., not significant, *$p < 0.05$, two-way repeated measures ANOVA with Holm-Šídák's multiple comparisons post-hoc test). Data are represented as mean ± SEM.

11. Carrillo-Reid, L., Yang, W., Bando, Y., Peterka, D.S., and Yuste, R. (2016). Imprinting and recalling cortical ensembles. Science *353*, 691–694. https://doi.org/10.1126/science.aaf7560.

12. Carrillo-Reid, L., Han, S., Yang, W., Akrouh, A., and Yuste, R. (2019). Controlling visually guided behavior by holographic recalling of cortical ensembles. Cell *178*, 447–457.e5. https://doi.org/10.1016/j.cell.2019.05.045.

13. Marshel, J.H., Kim, Y.S., Machado, T.A., Quirin, S., Benson, B., Kadmon, J., Raja, C., Chibukhchyan, A., Ramakrishnan, C., Inoue, M., et al. (2019). Cortical layer-specific critical dynamics triggering perception. Science *365*, eaaw5202. https://doi.org/10.1126/science.aaw5202.

14. Wenzel, M., Han, S., Smith, E.H., Hoel, E., Greger, B., House, P.A., and Yuste, R. (2019). Reduced repertoire of cortical microstates and neuronal ensembles in medically induced loss of consciousness. Cell Syst. *8*, 467–474.e4. https://doi.org/10.1016/j.cels.2019.03.007.

15. Nir, Y., Massimini, M., Boly, M., and Tononi, G. (2013). Sleep and consciousness. In Neuroimaging of Consciousness, A. Cavanna, A. Nani, H. Blumenfeld, and S. Laureys, eds. (Springer), pp. 133–182. https://doi.org/10.1007/978-3-642-37580-4_9.

16. Kim, J.-Y., Grunke, S.D., Levites, Y., Golde, T.E., and Jankowsky, J.L. (2014). Intracerebroventricular viral injection of the neonatal mouse brain for persistent and widespread neuronal transduction. JoVE *91*, 51863. https://doi.org/10.3791/51863.

17. Dard, R.F., Leprince, E., Denis, J., Rao-Balappa, S., Suchkov, D., Boyce, R., Lopez, C., Giorgi-Kurz, M., Szwagier, T., Dumont, T., et al. (2022). The rapid developmental rise of somatic inhibition disengages hippocampal dynamics from self-motion. Elife *11*, e78116. https://doi.org/10.7554/eLife.78116.

18. Boyce, R., Glasgow, S.D., Williams, S., and Adamantidis, A. (2016). Causal evidence for the role of REM sleep theta rhythm in contextual memory consolidation. Science *352*, 812–816. https://doi.org/10.1126/science.aad5252.

19. Steriade, M., Timofeev, I., and Grenier, F. (2001). Natural waking and sleep states: a view from inside neocortical neurons. J. Neurophysiol. *85*, 1969–1985. https://doi.org/10.1152/jn.2001.85.5.1969.

20. Hudetz, A.G., Vizuete, J.A., Pillay, S., and Mashour, G.A. (2016). Repertoire of mesoscopic cortical activity is not reduced during anesthesia. Neuroscience *339*, 402–417. https://doi.org/10.1016/j.neuroscience.2016.10.023.

21. Lewis, L.D., Weiner, V.S., Mukamel, E.A., Donoghue, J.A., Eskandar, E.N., Madsen, J.R., Anderson, W.S., Hochberg, L.R., Cash, S.S., Brown, E.N., and Purdon, P.L. (2012). Rapid fragmentation of neuronal networks at the onset of propofol-induced unconsciousness. Proc. Natl. Acad. Sci. USA *109*, E3377–E3386. https://doi.org/10.1073/pnas.1210907109.

22. Barttfeld, P., Uhrig, L., Sitt, J.D., Sigman, M., Jarraya, B., and Dehaene, S. (2015). Signature of consciousness in the dynamics of resting-state brain activity. Proc. Natl. Acad. Sci. USA *112*, 887–892. https://doi.org/10.1073/pnas.1418031112.

23. Hudetz, A.G., Liu, X., and Pillay, S. (2015). Dynamic repertoire of intrinsic brain states is reduced in propofol-induced unconsciousness. Brain Connect. *5*, 10–22. https://doi.org/10.1089/brain.2014.0230.

24. Lehmann, D., Ozaki, H., and Pal, I. (1987). EEG alpha map series: brain micro-states by space-oriented adaptive segmentation. Electroencephalogr. Clin. Neurophysiol. *67*, 271–288. https://doi.org/10.1016/0013-4694(87)90025-3.

25. Pascual-Marqui, R.D., Michel, C.M., and Lehmann, D. (1995). Segmentation of brain electrical activity into microstates: model estimation and validation. IEEE Trans. Biomed. Eng. *42*, 658–665. https://doi.org/10.1109/10.391164.

26. Mégevand, P., Quairiaux, C., Lascano, A.M., Kiss, J.Z., and Michel, C.M. (2008). A mouse model for studying large-scale neuronal networks using EEG mapping techniques. Neuroimage *42*, 591–602. https://doi.org/10.1016/j.neuroimage.2008.05.016.

27. Michel, C.M., and Koenig, T. (2018). EEG microstates as a tool for studying the temporal dynamics of whole-brain neuronal networks: a review. Neuroimage *180* (*Pt B*), 577–593. https://doi.org/10.1016/j.neuroimage.2017.11.062.

28. Lehmann, D., Strik, W.K., Henggeler, B., Koenig, T., and Koukkou, M. (1998). Brain electric microstates and momentary conscious mind states as building blocks of spontaneous thinking: I. Visual imagery and abstract thoughts. Int. J. Psychophysiol. *29*, 1–11. https://doi.org/10.1016/s0167-8760(97)00098-6.

29. Milz, P., Faber, P.L., Lehmann, D., Koenig, T., Kochi, K., and Pascual-Marqui, R.D. (2016). The functional significance of EEG microstates-Associations with modalities of thinking. Neuroimage *125*, 643–656. https://doi.org/10.1016/j.neuroimage.2015.08.023.

30. Seitzman, B.A., Abell, M., Bartley, S.C., Erickson, M.A., Bolbecker, A.R., and Hetrick, W.P. (2017). Cognitive manipulation of brain electric microstates. Neuroimage *146*, 533–543. https://doi.org/10.1016/j.neuroimage.2016.10.002.

31. Santarnecchi, E., Khanna, A.R., Musaeus, C.S., Benwell, C.S.Y., Davila, P., Farzan, F., Matham, S., Pascual-Leone, A., and Shafi, M.M.; Honeywell SHARP Team authors (2017). EEG microstate correlates of fluid intelligence and response to cognitive training. Brain Topogr. *30*, 502–520. https://doi.org/10.1007/s10548-017-0565-z.

32. Musso, F., Brinkmeyer, J., Mobascher, A., Warbrick, T., and Winterer, G. (2010). Spontaneous brain activity and EEG microstates. A novel EEG/fMRI analysis approach to explore resting state networks. Neuroimage *52*, 1149–1161. https://doi.org/10.1016/j.neuroimage.2010.01.093.

33. Britz, J., Van de Ville, D., and Michel, C.M. (2010). BOLD correlates of EEG topography reveal rapid resting-state network dynamics. Neuroimage *52*, 1162–1170. https://doi.org/10.1016/j.neuroimage.2010.02.052.

34. Yuan, H., Zotev, V., Phillips, R., Drevets, W.C., and Bodurka, J. (2012). Spatiotemporal dynamics of the brain at rest-exploring EEG microstates as electrophysiological signatures of BOLD resting state networks. Neuroimage *60*, 2062–2072. https://doi.org/10.1016/j.neuroimage.2012.02.031.

35. Pascual-Marqui, R.D., Lehmann, D., Faber, P., Milz, P., Kochi, K., Yoshimura, M., Nishida, K., Isotani, T., and Kinoshita, T. (2014). The resting microstate networks (RMN): cortical distributions, dynamics, and frequency specific information flow. Preprint at arXiv. https://doi.org/10.48550/arXiv.1411.1949.

36. Custo, A., Van De Ville, D., Wells, W.M., Tomescu, M.I., Brunet, D., and Michel, C.M. (2017). Electroencephalographic resting-state networks: source localization of microstates. Brain Connect. *7*, 671–682. https://doi.org/10.1089/brain.2016.0476.

37. Milz, P., Pascual-Marqui, R.D., Achermann, P., Kochi, K., and Faber, P.L. (2017). The EEG microstate topography is predominantly determined by intracortical sources in the alpha band. Neuroimage *162*, 353–361. https://doi.org/10.1016/j.neuroimage.2017.08.058.

38. Mishra, A., Marzban, N., Cohen, M.X., and Englitz, B. (2021). Dynamics of neural microstates in the VTA-striatal-prefrontal loop during novelty exploration in the rat. J. Neurosci. *41*, 6864–6877. https://doi.org/10.1523/JNEUROSCI.2256-20.2021.

39. Irisawa, S., Isotani, T., Yagyu, T., Morita, S., Nishida, K., Yamada, K., Yoshimura, M., Okugawa, G., Nobuhara, K., and Kinoshita, T. (2006). Increased omega complexity and decreased microstate duration in nonmedicated schizophrenic patients. Neuropsychobiology *54*, 134–139. https://doi.org/10.1159/000098264.

40. Kikuchi, M., Koenig, T., Wada, Y., Higashima, M., Koshino, Y., Strik, W., and Dierks, T. (2007). Native EEG and treatment effects in neuroleptic-naive schizophrenic patients: time and frequency domain approaches. Schizophr. Res. *97*, 163–172. https://doi.org/10.1016/j.schres.2007.07.012.

41. Koenig, T., Lehmann, D., Merlo, M.C., Kochi, K., Hell, D., and Koukkou, M. (1999). A deviant EEG brain microstate in acute, neuroleptic-naive schizophrenics at rest. Eur. Arch. Psychiatr. Clin. Neurosci. *249*, 205–211. https://doi.org/10.1007/s004060050088.

42. Lehmann, D., Faber, P.L., Galderisi, S., Herrmann, W.M., Kinoshita, T., Koukkou, M., Mucci, A., Pascual-Marqui, R.D., Saito, N., Wackermann, J., et al. (2005). EEG microstate duration and syntax in acute, medication-naive, first-episode schizophrenia: a multi-center study. Psychiatr. Res. *138*, 141–156. https://doi.org/10.1016/j.pscychresns.2004.05.007.

43. Nishida, K., Morishima, Y., Yoshimura, M., Isotani, T., Irisawa, S., Jann, K., Dierks, T., Strik, W., Kinoshita, T., and Koenig, T. (2013). EEG microstates associated with salience and frontoparietal networks in frontotemporal dementia, schizophrenia and Alzheimer's disease. Clin. Neurophysiol. *124*, 1106–1114. https://doi.org/10.1016/j.clinph.2013.01.005.

44. Strelets, V., Faber, P.L., Golikova, J., Novototsky-Vlasov, V., Koenig, T., Gianotti, L.R.R., Gruzelier, J.H., and Lehmann, D. (2003). Chronic schizophrenics with positive symptomatology have shortened EEG microstate durations. Clin. Neurophysiol. *114*, 2043–2051. https://doi.org/10.1016/s1388-2457(03)00211-6.

45. Andreou, C., Faber, P.L., Leicht, G., Schoettle, D., Polomac, N., Hanganu-Opatz, I.L., Lehmann, D., and Mulert, C. (2014). Resting-state connectivity in the prodromal phase of schizophrenia: insights from EEG microstates. Schizophr. Res. *152*, 513–520. https://doi.org/10.1016/j.schres.2013.12.008.

46. Tomescu, M.I., Rihs, T.A., Becker, R., Britz, J., Custo, A., Grouiller, F., Schneider, M., Debbané, M., Eliez, S., and Michel, C.M. (2014). Deviant dynamics of EEG resting state pattern in 22q11.2 deletion syndrome adolescents: a vulnerability marker of schizophrenia? Schizophr. Res. *157*, 175–181. https://doi.org/10.1016/j.schres.2014.05.036.

47. Kindler, J., Hubl, D., Strik, W.K., Dierks, T., and Koenig, T. (2011). Resting-state EEG in schizophrenia: auditory verbal hallucinations are related to shortening of specific microstates. Clin. Neurophysiol. *122*, 1179–1182. https://doi.org/10.1016/j.clinph.2010.10.042.

48. Grieder, M., Koenig, T., Kinoshita, T., Utsunomiya, K., Wahlund, L.O., Dierks, T., and Nishida, K. (2016). Discovering EEG resting state alterations of semantic dementia. Clin. Neurophysiol. *127*, 2175–2181. https://doi.org/10.1016/j.clinph.2016.01.025.

49. Drissi, N.M., Szakács, A., Witt, S.T., Wretman, A., Ulander, M., Ståhlbrandt, H., Darin, N., Hallböök, T., Landtblom, A.M., and Engström, M. (2016). Altered brain microstate dynamics in adolescents with narcolepsy. Front. Hum. Neurosci. *10*, 369. https://doi.org/10.3389/fnhum.2016.00369.

50. Kikuchi, M., Koenig, T., Munesue, T., Hanaoka, A., Strik, W., Dierks, T., Koshino, Y., and Minabe, Y. (2011). EEG microstate analysis in drug-naive patients with panic disorder. PLoS One *6*, e22912. https://doi.org/10.1371/journal.pone.0022912.

51. Gschwind, M., Hardmeier, M., Van De Ville, D., Tomescu, M.I., Penner, I.K., Naegelin, Y., Fuhr, P., Michel, C.M., and Seeck, M. (2016). Fluctuations of spontaneous EEG topographies predict disease state in relapsing-remitting multiple sclerosis. Neuroimage. Clin. *12*, 466–477. https://doi.org/10.1016/j.nicl.2016.08.008.

52. Corradini, P.L., and Persinger, M.A. (2014). Spectral power, source localization and microstates to quantify chronic deficits from 'mild' closed head injury: correlation with classic neuropsychological tests. Brain Inj. *28*, 1317–1327. https://doi.org/10.3109/02699052.2014.916819.

53. Gao, F., Jia, H., Wu, X., Yu, D., and Feng, Y. (2017). Altered resting-state EEG microstate parameters and enhanced spatial complexity in male adolescent patients with mild spastic diplegia. Brain Topogr. *30*, 233–244. https://doi.org/10.1007/s10548-016-0520-4.

54. Zappasodi, F., Croce, P., Giordani, A., Assenza, G., Giannantoni, N.M., Profice, P., Granata, G., Rossini, P.M., and Tecchio, F. (2017). Prognostic value of EEG microstates in acute stroke. Brain Topogr. *30*, 698–710. https://doi.org/10.1007/s10548-017-0572-0.

55. Pnevmatikakis, E.A., and Giovannucci, A. (2017). NoRMCorre: an online algorithm for piecewise rigid motion correction of calcium imaging data. J. Neurosci. Methods *291*, 83–94. https://doi.org/10.1016/j.jneumeth.2017.07.031.

56. Halász, P., Terzano, M., Parrino, L., and Bódizs, R. (2004). The nature of arousal in sleep. J. Sleep Res. *13*, 1–23. https://doi.org/10.1111/j.1365-2869.2004.00388.x.

57. Chronux Analysis Software. http://chronux.org/.

58. Mitra, P., and Bokil, H. (2008). Observed Brain Dynamics (Oxford University Press).

59. Feldt-Muldoon, S., Soltesz, I., and Cossart, R. (2013). Spatially clustered neuronal assemblies comprise the microstructure of synchrony in chronically epileptic networks. Proc. Natl. Acad. Sci. USA *110*, 3567–3572. https://doi.org/10.1073/pnas.1216958110.

STAR★METHODS

KEY RESOURCES TABLE

REAGENT or RESOURCE	SOURCE	IDENTIFIER
Bacterial and virus strains		
AAV1-hSyn-GCaMP6s.WPRE.SV40	Addgene	Viral prep #100843-AAV1; RRID: Addgene_100843
Experimental models: Organisms/strains		
Mouse: Swiss Webster (CFW)	C.E Janvier	SW-F/SW-M
Software and algorithms		
MATLAB	MathWorks	MATLAB R2017b
GraphPad Prism	Dotmatics	Prism 9.3.1
NoRMCorre	Pnevmatikakis and Giovannucci, 2017[55]	https://github.com/flatironinstitute/NoRMCorre
Chronux signal processing toolbox	http://chronux.org/	Chronux version 2.12

RESOURCE AVAILABILITY

Lead contact

Further information and requests for resources and reagents should be directed to and will be fulfilled by the lead contact, Richard Boyce (rboyce54@gmail.com).

Materials availability

This study did not generate any unique reagents.

Data and code availability

- All data reported in this paper will be shared by the lead contact upon request.
- This paper does not report original code.
- Any additional information required to reanalyze the data reported in this work paper is available from the lead contact upon request.

EXPERIMENTAL MODEL AND SUBJECT DETAILS

All experimental procedures were approved by the French ethics committee (Ministère de l'Enseignement Supérieur, de la Recherche et de l'Innovation (MESRI); Comité d'éthique CEEA-014; APAFiS #'s 18.185, 28.506) and were conducted in agreement with the European Council Directive 86/609/EEC. Male Swiss wild-type mice (C.E. Janvier, France) were used in this study. With the exception of neonatal (P0) virus injections, all experimental procedures were performed in adult mice which were at least 3 months old. When not being used in experiments, mice were housed in cages on a 12h:12h light:dark light schedule (lights on at 20:00 h) and had access to food and water *ad libitum*. Mice were housed in individual cages following weaning at 3 weeks age.

METHOD DETAILS

Virally-mediated expression of calcium indicators

In-vivo calcium imaging experiments were facilitated through cortical expression of GCaMP6s via the viral vector AAV1-hSyn-GCaMP6s.WPRE.SV40 (a gift from Douglas Kim & GENIE Project (Addgene viral prep #100843-AAV1; http://n2t.net/addgene:100843; RRID:Addgene_100843)). To achieve stable widespread GCaMP6s expression long-term throughout the cortex, we used an intracerebroventricular injection protocol.[16,17] On postnatal day 0, Swiss mouse pups were anesthetized on ice for 3–4 min and 2 μL of viral solution (titration at least 1 × 1013 vg/mL) were injected in the left lateral ventricle whose coordinates were estimated at 2/5 of the imaginary line between the lambda and the eye at a depth of 0.4 mm.

Implantation of electrodes and imaging window

At approximately 3 months age, transduced male mice were anesthetized with isoflurane (5% induction, 1–2% maintenance) and placed into a stereotaxic frame. Skin covering the top of the skull was removed and the skull surface was cleared of all connective tissue. The

head position was subsequently adjusted so that the bregma and lambda were located in the same horizontal plane. The top of the skull was then lightly scored with a drill and a thin layer of dental cement (C&B Metabond, Parkell, Edgewood, NY) was applied to the skull surface. In all of the mice, a ~250 μm diameter hole was drilled through the skull (anterior-posterior (AP) −2.67, medial-lateral (ML) +1.54, all values in mm relative to bregma) and a stainless-steel EEG screw (Antrin Miniature Specialities, Inc.) with an insulated tungsten wire lead (A-M systems; item # 795500) soldered to the screw head was inserted just until secure to avoid damaging the underlying dura. 2 additional screws were similarly placed in the bone above the frontal cortex and cerebellum to serve as ground and reference electrodes, respectively. In order to investigate the dynamics of global brain EEG microstates, 8 additional EEG screws (multi-EEGs) were added at the following coordinates in a subset of the mice: (AP +2.67, ML ± 1.54; AP 0.00, ML 0.00, ±3.08; AP -2.67, ML -1.54, ±4.62). In addition, an insulated stranded wire (Medwire) was inserted into the nuchal muscle to serve as an electromyogram for recording of postural muscle tone. To facilitate 2-photon calcium imaging of cortical neural activity, a 3 mm diameter circular portion of the skull centered over the sensorimotor cortex of the left hemisphere (center coordinates: AP -0.75, ML -1.75) was then carefully removed. Next, a small amount of clear silicon polymer (Kwik-sil (World Precision Instruments)) was applied to the top of the dura and a 3 mm diameter glass window was subsequently placed on top. A metal bar, required for head-fixation of mice during later experiments, was placed at the back of the skull behind the cerebellar reference screw. Mill Max pins (Duratool corporation) soldered to the wire leads originating from the EEG, EMG, ground, and reference electrodes were then fixed in a precise configuration on top of the metal bar; pins were oriented toward the rear of the mouse at a vertical angle of 45° to keep enough space for the objective and also prevent the headstage preamplifier from obstructing the mouse when head fixed. As a final step, all electrodes were insulated and the entire implant was secured with additional dental cement. Mice were then returned to their home cage and given buprenorphine (0.1 mg/kg) to help with pain management during the initial recovery period. Mice were given 3 weeks to rest in order to ensure a full recovery from the surgery. At this time, the quality of the implanted electrodes and imaging field of view (FOV) was assessed; of 13 total mice that underwent the procedure outlined above, 6 were excluded from further experimentation at this point due to a poor FOV signal to noise ratio (due to low levels of GCaMP6s expression and/or the presence of debris or air pockets under the imaging window which interfered with the fluorescent signal below). In the remaining 7 mice, 4 of which had multi-EEG implants, the behavioral habituation procedure was started.

Habituation to head fixation

Once fully recovered from the electrode and imaging window implant procedure, habituation sessions for prolonged head fixation commenced. The start of each session occurred ~1 h before the start of the light cycle to encourage sleeping behavior. Using the metal bar attached to the head of the mouse during the prior surgery, mice were head fixed underneath the 2-photon microscope on a non-motorized treadmill that allowed them to run at will. Light in the room was kept to a minimum to prevent contamination of the imaging signal. For each mouse, a single dedicated tread was used for the entire duration of a given habituation and recording procedure. The head position was customized for each mouse to ensure that they would be able to sleep in a sphinxlike position on the tread while leaving enough space to allow for running. Mice participated in 1 training session per day, with the duration of head fixation being gradually increased across 12 successive sessions to a maximum duration of 4.5 h: 5 min, 15 min, 30 min, 45 min, 1 h, 1.5 h, 2 h, 2.5 h, 3 h, 3.5 h, 4 h, 4.5 h. Once the maximum duration of 4.5 h was reached, the daily head fixation time remained constant until the experiment endpoint was reached. This procedure was tolerated well by all mice used in this study; all but 1 of the 7 remaining mice demonstrated a consistent full sleep-wake cycle (wakefulness, NREMs, REMs) while head fixed that was relatively stable from day-to-day ~4 weeks after starting habituation. The remaining mouse tolerated the procedure well; however, as there was little sustained (>5 s continuous) sleep activity, it was excluded from any further data acquisition and analysis. Sessions were completed daily throughout the duration of an experiment for a given mouse (habituation and subsequent data acquisition), unless mice began to demonstrate signs of fatigue (significant (>50%) decrease in sleep quantity and weight loss (more than 5%) relative to prior day), in which case they were allowed to rest at least 1 day or until weight recovered (typically 1–2 days), respectively. ~2 weeks of data acquisition was typically required for a given mouse to obtain a single experiment with optimal quality imaging and EEG data as a result of common logistical issues related to imaging (primarily loss of imaging FOV mid-experiment due to bubble formation or a shift in the FOV position that could not be corrected post-hoc). For each mouse, only data from a single optimal experiment was used for subsequent data preprocessing and analysis steps. Finally, to assess the potential impact of head fixation on sleep quality, the day following completion of data acquisition, the treadmill apparatus was removed from the 2-photon imaging platform and replaced by an empty cage with woodchip bedding. The mouse was placed un-head fixed in the cage with the head stage pre-amplifier tether attached, and was subsequently recorded under otherwise identical experimental conditions (i.e., at the same time, for the same duration, under the same lighting conditions, and with the microscope scanner active). Once this endpoint was reached, mice were utilized for experiments in an unrelated project.

Electrophysiological recording

Electrophysiological recordings were done during all phases of the experiment (head-fixation habituation in order to track habituation progression as well as during imaging data acquisition experiments in fully habituated mice). For each recording, a head stage pre-amplifier (Neuralynx, Boseman, Montana, USA) tether was attached to the Mill-max connector pins at the rear of the head of the mouse immediately after being head fixed into the 2-photon imaging setup. Data from all electrodes were subsequently amplified by the head stage pre-amplifier before being digitized at 16,000 Hz using a digital acquisition system (Neuralynx, Boseman, Montana, USA) and saved to a hard disk. Tread movement was also captured through a video recording synchronized to the electrophysiology data.

2-Photon imaging of cortical neural activity

To keep the size of datasets manageable and minimize the potential for photobleaching, imaging data acquisition was limited to the second half of the experiment (~2.25 h in duration, hour 2.25–4.5 of experiment) when sleep activity was generally highest. At the start of this period, a 16× immersion objective (NIKON, NA 0.8) connected to a GaSP PMT (H7422-40, Hamamatsu) was positioned over the imaging region of interest (field of view (FOV)) within the sensorimotor cortex at an imaging depth corresponding to ~150–250 μm below the pial surface. A series of 25 movies (2500 frames per movie acquired at 8 Hz (thus each movie has a duration of ~5 min 12 s with ~12 s interval between consecutive movies), FOV size = 400 × 400 μm acquired at a resolution of 200 × 200 pixels) was obtained using a single beam multiphoton-pulsed laser scanning system coupled to a microscope (TriM Scope II, LaVision Biotech) and Ti: sapphire excitation laser (Chamelon Ultra II, Coherent) operated at 920 nm. GCamp6s fluorescence was isolated using a bandpass filter of 510 nm/25nm. Images were acquired from the PMT signal using Imspector software (LaVision, Biotech) and subsequently saved to a hard disk. There was no evidence of photo-toxicity or significant bleaching as a result of the above imaging procedure. To synchronize imaging data with electrophysiological data, a TTL timestamp signal was sent from the imaging acquisition software to the digital electrophysiology acquisition system at the onset of each imaging frame scanning cycle.

Data analysis

All following data analysis was performed using custom written scripts in MATLAB (The MathWorks, Inc.).

Vigilance state architecture analysis

For quantitative and qualitative analysis of sleep and wake activity of each experiment, raw EEG and electromyogram data files were first imported into MATLAB and downsampled to 1000 Hz. Data was then manually plotted and the major phases of the sleep-wake cycle occurring throughout the entire recording session were scored in 5 s epochs using the fast Fourier transform (FFT; 'fft' function in MATLAB) of the signal recorded from the right parietal EEG (AP -2.67, ML +1.54) in addition to the nuchal EMG signal.[18] The procedure was as follows: epochs of wakefulness were identified by a binned 'theta' (4–10 Hz, 'θ') to 'delta' (1–4 Hz, 'δ') power ratio greater than 1 and bursts of relatively high-amplitude movement-associated EMG activity (typically >0.1 mV and >1 s in duration). Epochs of NREMs were identified by a binned θ/δ power ratio <1 and a lack of high-amplitude EMG activity. Transient spindle (9–15 Hz) oscillations were also observed periodically during NREMs. Epochs of REMs followed and preceded NREMs and wakefulness, respectively, and were identified by a binned θ/δ power ratio greater than 1 and a completely flat EMG signal except for relatively brief and phasic (<1 s in duration) periods of high-amplitude EMG activity associated with muscle twitches. While many state transitions were relatively gradual, occurring over the course of several epochs (e.g., from wakefulness to NREMs, NREMs to REMs) and thus allowing the above criteria to be applied with ease, epochs during which clear and relatively abrupt state transitions occurred (e.g., REMs to wakefulness) were scored as being the state that occupied the majority of the epoch. Once scoring was completed, the data was manually reviewed and crosschecked with video recordings to ensure a perfect correspondence between overt mouse behavior (e.g., movement, grooming) and the scored vigilance state data (hypnogram). This step included removing large microarousals occurring during NREMs,[56] characterized by a transient and sudden reduction of high-amplitude slow wave activity concomitant with an increase in low-amplitude high-frequency activity and increased muscle tone. This was done as a safeguard to prevent the inadvertent inclusion of brief awakenings in NREMs data selected for later analysis. Total state proportions and average state durations for each experiment were calculated based on the hypnograms generated using the above procedure.

For EEG microstate and imaging data analysis, periods of wakefulness were further segregated into 'active wake' or 'quiet wake' according to the presence or absence of movement-associated activity bursts in the EMG signal, respectively. Thus, quiet wake periods were completely free of both running and other active behaviors, such as grooming. To ensure that periods of early transitional sleep were not accidentally identified as quiet wake, only periods of quiet wake completely free of any events reminiscent of large slow wave and spindle-like activity that were flanked by overt periods of active wakefulness were selected. As a final step, potential periods of active wake identified in the prior step were cross-checked with tread movement data to enable removal of all time points which did not correspond to periods of running behavior (e.g., grooming behavior).

Spectral analysis of EEG data

For analyses that prioritized frequency resolution (creation of basic EEG spectrograms, spectral analysis of EEG microstate dynamics), vigilance state-specific spectral analysis of EEG data was completed in MATLAB using the mtspecgramc function from the Chronux signal processing toolbox (parameters: window size = 5 s, step size = 5 s, tapers [3 5]).[57,58]

Wavelet analysis of EEG data

For analyses that prioritized temporal resolution (correlation of specified frequency bands with EEG microstate dynamics), vigilance state-specific Morlet wavelet analysis of EEG data was completed in MATLAB using the 'cwt' function. The absolute values of the resulting complex wavelet transforms were then calculated for each time point, and data were binned according to the following non-overlapping frequency definitions: 'delta' (1–4 Hz, δ); 'theta' (4–10 Hz, θ); 'alpha' (10–15 Hz, α); 'beta' (15–30 Hz, β); 'gamma' (30–50 Hz). Values originating from datapoints within 0.5 s of a temporal break in the data were ignored.

EEG microstate analysis

To gain insight into global brain activity dynamics, we opted to employ EEG microstate analysis as this procedure could be incorporated into our cortical imaging protocol with relative ease as opposed to other potential techniques (e.g., fMRI). For identification of EEG microstates, we used a protocol similar to a well-established procedure.[25,27] EEG traces from each experiment were first bandpass filtered from 1–50 Hz using the 'filtfilt' function in MATLAB. The 'global standard deviation' (GSD), the standard deviation of all EEG signals, was then calculated for each data time point and the indices of peak locations in the GSD were subsequently found using the 'findpeaks' function in MATLAB. For each experiment, equal amounts of quiet wake, NREMs, and REMs data that were free of activity bursts in the EMG were then identified. Periods of active wake were not analyzed due to the high potential for contamination of EEG signals with movement artifacts. The amount of data available for each state was therefore limited by the state with the least amount of data available (typically REMs). Valid data points for other states that had to be excluded as a result were removed at random. The EEG profile maps, the instantaneous potential of each EEG signal, associated with the indices of each identified peak in the GSD occurring during identified EMG noise-free quiet wake, NREMs, and REMs periods were then clustered separately as well as in combination (i.e., select quiet wake, NREMs, and REMs periods combined) using the k means clustering 'kmeans' function in MATLAB (parameters: maximum number of clusters = 10, number of iterations per clustering step = 100), followed by silhouette analysis using the MATLAB 'silhouette' function. For statistical evaluation of clustering results, the above procedure was repeated 100 x using shuffled surrogate data which was generated by shifting each EEG channel individually relative to their initial position by a random amount. The resulting outcomes of clustering were highly similar both for different states (including all states combined condition) within a single experiment as well as between different experiments, consistent with prior reports.[25,27] Therefore, to best facilitate comparison of microstate dynamics between different states, the optimal cluster number that was subsequently used for state-specific microstate analysis was set at that which produced an explained variance closest to 90% in clustering of combined (select quiet wake, NREMs, and REMs) data. This approach was used instead of taking the cluster number associated with the peak silhouette value in order to capture the maximum reasonable amount of variation in the data. For each individual state (select quiet wake, NREMs, and REMs) of each experiment, the clustering results associated with the optimal cluster number determined using the aforementioned procedure were statistically significant (silhouette value higher value than that from at least 95/100 of the shuffled surrogates). As a final step, EEG profile template 'maps' were generated for every individual cluster by averaging, for each EEG, the potentials associated with all constituent timepoints of the cluster. Potential maps corresponding to each cluster were then reindexed according to their general features which were consistently observed both within (i.e., different vigilance states within the same animal) and between experiments (i.e., different mice). Potential 'Map 1' was characterized by relatively increased potentials in the frontal and posterior electrodes. 'Map 2' was also characterized by relatively increased potentials in the frontal and posterior electrodes; however, the profile was shifted more negatively relative to those of 'Map 1'. 'Map 3' was characterized by relatively increased potentials in the middle EEG electrodes, while 'Map 4' was also characterized by relatively increased potentials in the middle EEG electrodes but shifted more negatively relative to those of 'Map 3'.

Although a cluster number of 4 was consistently suggested as optimal according to our criteria outlined above, we also performed the primary analysis of our study (i.e., Figure 4) using a cluster number of 2 for EEG microstate identification since the apparent co-occurrence of microstate maps 1 and 3 as well as 2 and 4 that is occasionally observed in the data (e.g., Figure 3B) might suggest a better fit of the data with 2 clusters. While less refined, the results were essentially the same as those obtained using a cluster number of 4 (Figure S8), indicating that our results are robust when using a cluster number of either 2 or 4 (i.e., are robust to moderate changes in the degree of fitting of the data).

Construction of topographical maps of multi-EEG potentials

Topographical maps used to depict the spatial organization of multi-EEG potentials at various time points were constructed by first plotting the corresponding derived potential values of each constituent EEG (i.e., EEG # 1–9) in 2 dimensions with accurate spatial relation to one another, then interpolating the intervening values. 2-dimensional maps were then placed, at accurate scale, over dorsal view schematics of the skull. Topographical maps corresponding to significant identified EEG microstates were frequently scaled according to the max-min difference for each map individually to enable visualization of variations in topographical potentials within each given map; in these cases, direct comparison of values between each individual map is possible due to the inclusion of accompanying linear plots (see figure legends for details).

Analysis of spindle activity in multi-EEG data

Spindle analysis was completed on temporally continuous periods of select NREMs data (the same periods used for EEG microstate analysis during NREMs) using non-overlapping 100 ms windows; the following procedure was completed for each EEG channel individually. For each window, EEG data was first bandpass filtered (9–15 Hz) using the 'filtfilt' function in MATLAB. The data was then rectified and the sum of the absolute amplitude values was calculated. The mean and standard deviation (stdev) of absolute amplitude data values derived from all analysis windows was subsequently obtained and used to determine the threshold for spindle detection (mean +3 stdev). All time points associated with values exceeding this threshold were considered to be locations of significant spindle activity.

Motion correction of imaging data

Raw imaging movies for each experiment were first loaded into MATLAB, concatenated into a single 3-dimensional matrix, and subjected to motion correction using the NoRMCorre algorithm.[55] The procedure consisted of 2 rounds of rigid motion correction with successively stricter corrective parameters (bin size of 10 and maximum allowable shift of 30 for the first round; bin size of 2 with a maximum allowable shift of 15 for the second round). This was followed by 2 rounds of non-rigid motion correction, also with successively stricter corrective parameters (grid size of ¼ the imaging field of view, bin size of 3, and maximum allowable shift of 15 for the first round; grid size of 1/8 the imaging field of view, bin size of 2, and a maximum allowable shift of 10 for the second round). Following the above motion correction procedure, the final corrected movie was visualized with the un-corrected data and manually scanned to ensure the absence of significant overcorrections and/or other artifacts resulting from the algorithm.

Determination of neurons (regions of interest) in imaging field of view

The identification of regions of interest (ROIs) corresponding to neurons in the field of view (FOV) of motion corrected movies was completed using a semi-automated approach. Each motion corrected movie was manually played back frame-by-frame; during the playback, regions of interest (ROIs, i.e., areas of the field of view with calcium signals characteristic of healthy cortical neurons) were manually identified. When a ROI was identified, a pixel in the center of the ROI was manually selected as a 'seed'. The calcium signal of this seed pixel throughout the course of the full movie was then z-scored, and the similarity of this data vector was compared to that for each pixel in the immediate vicinity (pixels within 10 μm of the seed pixel) via linear correlation using the 'corr' function in MATLAB. Pixels whose activity during the movie was highly correlated ($p < 0.01$) with that of the seed pixel were automatically included as part of the ROI. If necessary, the pixels assigned to the ROI were then manually adjusted; adjustment was largely limited to the removal of pixels clearly associated with processes, as well as those overlapping/in direct juxtaposition with other cells. The above process was repeated until all clearly identifiable ROIs had been registered. At this point, a trace was derived for each ROI by averaging the calcium signal across all constituent pixels for each movie frame.

Identification of transient activity in calcium traces

Following extraction of calcium traces from identified ROIs, identification of calcium transients from this data was next completed for each experiment. For this, each raw calcium trace obtained from imaging data was first smoothed with a Gaussian filter using the 'smoothdata' function in MATLAB and a smoothing window size corresponding to 1 s of data (8 frames). The 'findpeaks' MATLAB function was then used to identify the location (time point), peak prominence, and width of peaks occurring in the smoothed trace. The onset timepoints for each peak were then identified by finding the closest preceding upwards deflection in the differentiated smoothed trace, calculated using the 'diff' function in MATLAB. Peaks corresponding to significant calcium transients were then automatically detected by determining those which had prominences greater than the set threshold value of 250 units. This threshold value was determined for the current experiments as follows; first, the mean and standard deviation of the raw calcium signal for all ROIs was calculated during quiescent periods of the recording (periods where the animal was not moving and no cells were active) for each mouse. The value of 250 units was the nearest whole value (50 unit resolution required to best facilitate manual verification of detected peaks described below) that was greater than 3 standard deviations above the average standard deviation calculated for the noisiest experiment. The raw and corresponding smoothed traces, along with the calculated locations of significant calcium transients, were then verified by plotting the data in an interactive figure and scanning through the entire trace. Manual corrections were able to be made at this time; these were largely limited to the exclusion of transients detected during periods contaminated with uncorrectable movement artifacts, as well as the inclusion of clear transients occurring in quick succession. Once detection and manual verification of transients was complete, the data was binarized into spike rasters; for each ROI, periods without significant transient activity were indicated with a 0, while the periods corresponding to significant transient activity (frames occurring between the onset and peak location calculated for each significant transient) were indicated with a 1. It is important to note that when using the above approach, sustained continuous inferred activity (i.e., activity lasting multiple imaging frames) of a given neuron does not imply continuous depolarization, but rather multiple consecutive spikes that are too fast to be resolved due to the relatively slow dynamics of calcium indicators in conjunction with the imaging frame rate. It is also important to emphasize that despite the relatively slow dynamics of our technique, this approach was nonetheless highly effective at capturing increases in cortical neural activity known to be associated with specific network events (e.g., EEG slow oscillations[19]; Figure S2).

Hierarchical clustering of cortical imaging data

To evaluate the presence of assemblies, defined in this study as neurons which coactive together, in cortical imaging data, we used a hierarchical clustering procedure.[59] Despite the disadvantage of being a relatively time-consuming technique compared to other clustering methods that could be used on this dataset, we opted to employ this clustering procedure on our imaging data due to the significant advantage of there being no need to predefine the number of clusters present. To enable a comparison of assembly activity between different vigilance states, equal amounts of active wake, quiet wake, NREMs, and REMs data were identified (note that for mice with multi-EEGs imaging data was synchronized with the same quiet wake, NREMs, and REMs data time points used for EEG microstate analysis described in the previous section). The amount of data available for each state was therefore limited by the state with the least amount of data available (typically REMs). For select imaging data obtained for each vigilance state within an individual experiment, the hierarchical clustering procedure was as follows. First, the 0-lag associated cross-correlation value for each

ROI pair was calculated using the 'xcorr' function in MATLAB and stored in a correlation matrix. The corresponding p value of the correlation between each ROI pair was then found through the use of a block-shuffling technique. This procedure, which was repeated 100 x for each ROI pair, involved fragmenting the spike rasters of both ROIs into ~5 s blocks and independently reassembling them in random order before calculating and storing the correlation value. Once this process had been repeated 100 x, the *p* value of the correlation value found between the intact spike rasters of the ROI pair was determined by calculating the proportion of correlation values corresponding to the shuffled surrogates that were weaker (smaller) than that calculated for the intact data. When the initial correlation and corresponding p-value matrices had been created, the main clustering procedure began. The index of the most statistically significant positive correlation in the entire matrix was found and the two associated ROIs were 'clustered' together with the corresponding spike rasters being merged. The values in the correlation matrix associated with the individual ROIs were nullified, and correlation and *p*-values were calculated between the newly merged spike raster and all of the remaining spike rasters. The index of the most statistically significant positive correlation in the entire matrix was again found and the associated ROIs (including correlations involving rasters that were the product of the merging of data from multiple ROIs) were clustered together. This process was repeated until there were no remaining significantly correlated spike raster pairs. At this point, the indices of ROIs (cortical neurons) that had been clustered together were stored. Only clusters consisting of at least 5 ROIs were considered valid in order to minimize the potential for chance cluster activations to introduce noise in subsequent analysis (i.e., dramatically reduce the likelihood that a single cluster could contain a proportionally significant number of neurons which were clustered together as a result of chance *p* values). For analysis of assembly activity, an assembly was considered active during a given frame if at least 3 of its constituent neurons were simultaneously active. Consecutive frames as well as frames that were not separated by a period where no constituent cells were active were not counted as unique assembly activations. Assembly start points were defined for each identified assembly activation as the time point at which the first constituent neuron became active. For all analyses, assembly activation start points identified with the above procedure which were located within 125 ms of a temporal break in the data were not analyzed due to potential prior activity.

The above clustering protocol was able to identify the presence of significant cluster (neural assembly) activity in all vigilance states tested for each mouse. Even so, a weakness of this clustering approach is the inability to assign a given neuron to more than 1 cluster. Therefore, any neurons which individually participate in multiple assemblies would not be identified in this study, an important potential caveat. However, the similarity of neural activity occurring during a specific vigilance state of a given experiment, assessed via Pearson correlation of activity rasters, was significantly higher between neurons belonging to the same assembly than for neurons originating from different assemblies (Figure S3A), indicating that different assemblies identified within the same vigilance state-specific data segment were generally highly distinct and non-overlapping. Finally, an important consideration surrounding our procedure for identifying cortical assembly activity is that, while it is a general method for detecting neurons which consistently coactivate together, it is not capable of segregating assembly activity arising from multiple different potential coactivation-promoting factors (e.g., [9]).

QUANTIFICATION AND STATISTICAL ANALYSIS

Unless stated otherwise within the text, statistical analysis was performed using GraphPad Prism software (Dotmatics). $p < 0.05$ was considered statistically significant, and all group-level data are presented as mean ± SEM. No subjects which reached the previously defined experimental endpoint, nor data values produced from resulting analysis, were excluded from this study. Where appropriate, the decision to use parametric vs non-parametric statistical measures was strictly dependent on the results of normality and equal means testing using the Kolmogorov-Smirnov and Bartlett's tests, respectively. Specific statistical details can be found in the figure legends, as well as in the 'method details' section for shuffling-based statistical analysis used for evaluation of clustering results.